


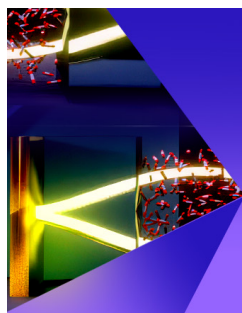
RESEARCH ARTICLE | APRIL 09 2020

# The ground and ionic states of cyclohepta-1,3,5-triene and their relationship to norcaradiene states: New $^1\text{H}$ and $^{13}\text{C}$ NMR spectra and analysis of a new experimental photoelectron spectrum by *ab initio* methods

Michael H. Palmer ; R. Alan Aitken ; Marcello Coreno ; Monica de Simone ; Cesare Grazioli ; Søren Vrønning Hoffmann ; Nykola C. Jones 



*J. Chem. Phys.* 152, 144301 (2020)  
<https://doi.org/10.1063/1.5142268>



The Journal of Chemical Physics

Special Topic:  
Polaritonics for Next Generation Materials

Submit Today



# The ground and ionic states of cyclohepta-1,3,5-triene and their relationship to norcaradiene states: New $^1\text{H}$ and $^{13}\text{C}$ NMR spectra and analysis of a new experimental photoelectron spectrum by *ab initio* methods

Cite as: J. Chem. Phys. 152, 144301 (2020); doi: 10.1063/1.5142268

Submitted: 11 December 2019 • Accepted: 6 March 2020 •

Published Online: 9 April 2020



View Online



Export Citation



CrossMark

Michael H. Palmer,<sup>1,a)</sup>  R. Alan Aitken,<sup>2,b)</sup>  Marcello Coreno,<sup>3,b)</sup>  Monica de Simone,<sup>4,b)</sup>   
Cesare Grazioli,<sup>4,b)</sup>  Søren Vrønning Hoffmann,<sup>5,b)</sup>  and Nykola C. Jones<sup>5,b)</sup> 

## AFFILIATIONS

<sup>1</sup>School of Chemistry, University of Edinburgh, Joseph Black Building, David Brewster Road, Edinburgh EH9 3FJ, Scotland, United Kingdom

<sup>2</sup>School of Chemistry, University of St Andrews, North Haugh, St Andrews Fife, St Andrews KY16 9ST, Scotland, United Kingdom

<sup>3</sup>ISM-CNR, Istituto di Struttura della Materia, LD2 Unit, 34149 Trieste, Italy

<sup>4</sup>IOM-CNR Laboratorio TASC, Trieste, Italy

<sup>5</sup>ISA, Department of Physics and Astronomy, Aarhus University, Ny Munkegade 120, DK-8000 Aarhus C, Denmark

<sup>a)</sup> Author to whom correspondence should be addressed: [m.h.palmer@ed.ac.uk](mailto:m.h.palmer@ed.ac.uk)

<sup>b)</sup> Electronic addresses: [raa@st-andrews.ac.uk](mailto:raa@st-andrews.ac.uk); [marcello.coreno@elettra.eu](mailto:marcello.coreno@elettra.eu); [desimone@iom.cnr.it](mailto:desimone@iom.cnr.it); [grazioli@iom.cnr.it](mailto:grazioli@iom.cnr.it); [vronning@phys.au.dk](mailto:vronning@phys.au.dk); and [nykj@phys.au.dk](mailto:nykj@phys.au.dk)

## ABSTRACT

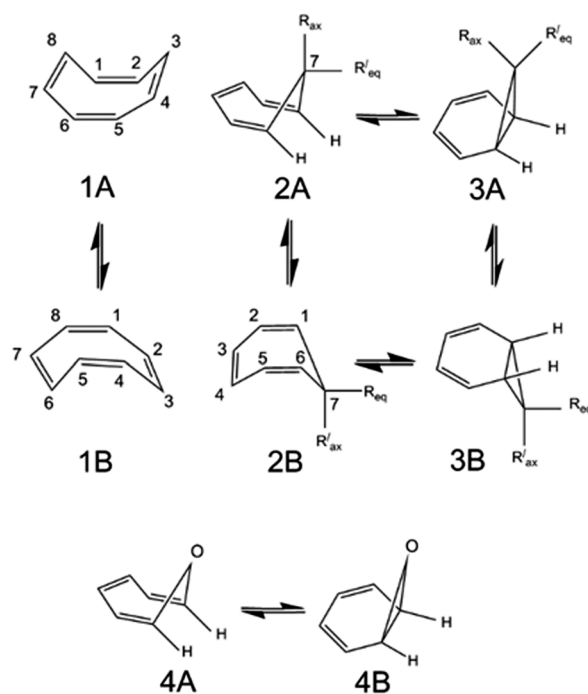
The strong inter-relationship between cyclohepta-1,3,5-triene (CHT) and norcaradiene (NCD) systems observed in some reactions has been extended to include the energy surfaces for some low-lying ionic states. Equilibrium structures for ionic states of CHT with  $^2A'$  symmetry were routinely found; the structures emerging with  $^2A''$  symmetry were NCD ionic states. A detailed analysis of these surfaces as a function of the  $C_1$  to  $C_6$  distance showed that while minima occurred for both state symmetries, curve crossing occurs in  $C_S$  symmetry, which is avoided by distortion to  $C_1$  symmetry. The CHT  $\rightarrow$  NCD structural change is attributed to initial conrotatory closure of the singly occupied molecular orbital. A new synchrotron-based photoelectron spectrum (PES) for CHT up to 25 eV shows little vibrational structure. We have assigned the PES up to 17 eV using a variety of theoretical methods. The calculated lowest ionic state,  $X^2A'$ , is predicted to have a very low vibrational frequency of  $87\text{ cm}^{-1}$ , leading to a high density of vibrational states. The Franck–Condon envelopes calculated for the two lowest states are almost completely contained within the envelope of the lowest PES band. A comparison of the predicted PES of CHT and NCD showed much closer agreement of the PES with that of CHT. An analysis of the  $^1\text{H}$  and  $^{13}\text{C}$  nuclear magnetic resonance (NMR) spectra of CHT showed no evidence of NCD. The increased chemical shifts arising from the higher frequencies used here lead to significant changes in appearance when compared with earlier NMR spectra.

Published under license by AIP Publishing. <https://doi.org/10.1063/1.5142268>

## I. INTRODUCTION

Recently, we reported a new high-resolution photoelectron spectrum (PES) and vacuum ultraviolet (VUV) spectra of cyclooctatetraene (COT);<sup>1,2</sup> this molecule undergoes  $D_{2d} \rightleftharpoons D_{2d}$  “tub to tub”

interconversions together with single  $\rightleftharpoons$  double bond switches, as shown in Fig. 1 (1A + 1B). We now present a related study on the PES and nuclear magnetic resonance (NMR) spectra of cyclohepta-1,3,5-triene ( $C_7H_8$ , abbreviated to CHT); this molecule undergoes rapid interconversion between two  $C_S$  symmetry conformers in



**FIG. 1.** Structural relationships between cyclooctatetraene (1A, 1B), cycloheptatriene (2A, 2B), and norcaradiene (3A, 3B); their relationship to oxepin (4A) and benzene oxide (4B).

a manner similar to COT, as shown in Fig. 1 (2A + 2B). Our synchrotron based, high-resolution PES of CHT is subjected to a detailed theoretical analysis; previous studies of the PES for CHT showed poor resolution and received a cursory analysis.<sup>3–8</sup> We will report a detailed analysis of the VUV spectrum of CHT in a future paper.

The primary aim of the current study is to present new spectra for both the NMR and PES; our NMR study replaces early measurements below 100 MHz by values at 300 MHz (<sup>1</sup>H) and 75.46 MHz for <sup>13</sup>C. Our much higher frequencies lead to a fundamental change in the appearance of the spectra, a result of the change in chemical shift to a coupling constant ( $\delta/J$ ) ratio by a factor of between 5 and 10 for <sup>1</sup>H spectra. This leads to much more certainty in the detailed assignments to the NMR spectra and accounts for the appearance of both the low and high frequency spectra.

Both CHT and cyclopentadiene (CPD) are classic cases of hyperconjugation<sup>9</sup> through the CH<sub>2</sub> group. However, there are major differences; planarity in these cases leads to a total of 8 $\pi$  and 6 $\pi$ -electrons (here denoted as  $n$ ), respectively, for CHT and CPD, where one pair arises from the CH<sub>2</sub> group A'' orbital. Thus, the Hückel ( $4n + 2$ ) rule<sup>10</sup> predicts a triplet state and a singlet state, respectively, for planar CHT and CPD. This favors hyperconjugation in the latter but not in the former. Nevertheless, the  $\pi$ -bond spatial proximity in CHT enables non-local effects such as cross-ring interactions, including bridging to transition metal carbonyls and related species.<sup>8,11</sup>

CHT exhibits a complex thermal and photochemical behavior. For example, thermal transfer of an H-atom from the 7-methylene group to the adjacent C<sub>1</sub> and C<sub>6</sub>-atoms occurs; however, this leads to an identical molecular species.<sup>12–14</sup> The same process also occurs photochemically but involves a dark state,<sup>15,16</sup> which we will investigate in our future VUV study.

Some reactions suggest that CHT is in equilibrium with a valence tautomer, norcaradiene (NCD; Fig. 1, 3A+3B), which is systematically known as bicyclo[4.1.0]heptadiene. The apparent absence of NCD in CHT samples has been demonstrated by both <sup>1</sup>H<sup>17–20</sup> and <sup>13</sup>C NMR evidence previously,<sup>21</sup> and this conclusion is also borne out by our NMR spectra below. However, we will demonstrate that NCD states are formed during the search for equilibrium structures of some CHT ionic states. Furthermore, direct evidence that CHT and NCD interconvert has been shown by UV spectroscopy.<sup>22</sup> The Diels–Alder reaction of CHT with tetracyanoethylene, (NC)<sub>2</sub>C=C(CN)<sub>2</sub>, leads to an NCD structural product.<sup>23,24</sup> This reaction is unimolecular in dienophile concentration, which shows that the CHT  $\rightleftharpoons$  NCD equilibrium is fast in comparison with adduct formation.<sup>23,24</sup> This type of reaction, leading to strained products, seems to be well established. Syntheses directed toward substituted CHT/NCD with electron withdrawing substituents (e.g., –CEN or –CF<sub>3</sub>) lead to both CHT and NCD isomers.<sup>25</sup> These interconversions are not unique since the corresponding oxygen containing compounds oxepin and benzene oxide, depicted in Fig. 1 (4A + 4B), show rapid isomerism at room temperature and can be distinguished<sup>26</sup> by their <sup>13</sup>C NMR spectra at –134°. All these studies<sup>22–24</sup> present compelling evidence that CHT and NCD interchanges can occur.

Investigations by imaging photoelectron photoion coincidence (PEPICO) spectroscopy<sup>27</sup> have suggested that the toluene cation (TOL<sup>+</sup>) undergoes irreversible isomerism to CHT<sup>+</sup> and that several subsequent processes occur through this common radical ion. However, the PES of CHT and TOL<sup>28</sup> are completely distinct, and this is true of other thermal and photochemical products of CHT.

While CHT and NCD do interchange in some reactions, both previous NMR and our current spectra demonstrate the nature of our sample. The higher signal-to-noise ratio in the current NMR study enabled a more detailed search for NCD signals, but none were found.

Unexpected cross-ring interactions that occur during an equilibrium structural search for some excited CHT ionic states are described below.

## II. METHODS

As in our COT studies,<sup>1,2</sup> we use a combination of multi-configuration self-consistent field (MCSCF), configuration interaction (CI), and other theoretical methods; each of these methods has specific uses, and no single procedure can offer us a complete analysis. Our methods supersede, both in accuracy of the spectral determination and in rigor of the interpretation, when compared with earlier analyses.

### A. The <sup>1</sup>H and <sup>13</sup>C NMR spectra

The <sup>1</sup>H NMR spectra were run at 300 MHz as a 5% solution in CDCl<sub>3</sub>; the <sup>13</sup>C NMR spectra were determined at 75.46 MHz also

as a 5% solution in  $\text{CDCl}_3$ . Both experimental spectra and simulations were processed using an iNMR reader (version 6.1.7). The dominance of CHT in the sample used for the PES is clear since the spectra clearly demonstrate the monocyclic triene character; these are simpler than early studies<sup>17–20</sup> owing to the  $\delta/J$  ratio being more favorable and have a much higher signal-to-noise ratio. The  $^1\text{H}$  and  $^{13}\text{C}$  chemical shifts (relative to  $\text{Me}_4\text{Si} = 0.0$  for  $^1\text{H}$  and  $\text{CDCl}_3 = 77.0$  for  $^{13}\text{C}$ ), reported in Table I, use the labeling of CHT in Fig. 1 (2A,2B), where C- and H-atoms share numbering (see the supplementary material, SM1). The assignment was unambiguously confirmed by means of 2D H–H (COSY) and H–C (HSQC) correlations (see the supplementary material, SM2). Starting from the aliphatic signal at 2.25 ppm (7-H), we have successive correlations to 5.37 ppm, 6.19 ppm, and 6.59 ppm making these, respectively, 1,6-H, 2,5-H, and 3,4-H. On the HSQC spectrum, these signals then correlate, respectively, with the  $^{13}\text{C}$  signals at 27.9, 120.7, 126.5, and 130.9 confirming the assignments, shown in Table I, which are in agreement with previous work.<sup>21</sup> The detailed form of the proton signals (Fig. 2) shows considerable complexity, but we were able to reproduce this with a good level of agreement, by simulation using the chemical shift values of Table I and the coupling constants in Table II. A comparison of the resulting simulated signals with experiment (supplementary material, SM3) shows agreement in the chemical shift values of all significant peaks to  $\pm 0.002$  ppm. When compared to the two previous studies reported over 50 years ago,<sup>19,20</sup> which used selective decoupling at 60 MHz, we have been

TABLE I.  $^1\text{H}$  and  $^{13}\text{C}$  NMR chemical shifts ( $\delta$ )/ppm.

Chemical shift ( $\delta$ ) (ppm)	HC <sub>7</sub> H	C <sub>1,6</sub> H	C <sub>2,5</sub> H	C <sub>3,4</sub> H
$^1\text{H}$	2.252	5.368	6.193	6.592
$^{13}\text{C}$	27.91	120.71	126.49	130.90

able to optimize the coupling constants in the simulation to achieve the best match to the 300 MHz spectrum. Although the three-bond coupling constants are in good agreement with the previous values in all four cases (Table II), we were able to achieve a better fit by adjusting the four-bond and five-bond coupling constants ( $^4J$  and  $^5J$ , respectively). Previous studies could only evaluate the sum of  $^4J_{1-3} + ^5J_{1-4}$ . We were able to separate the values as shown, and this had a significant effect on the profile of the H<sub>3,4</sub> signal at 6.59 ppm. We also achieved considerable improvement when mimicking the shape of the observed H<sub>2,5</sub> peaks by using a larger value for  $^4J_{2-7}$ ; similarly, introducing  $^4J_{1-6}$  at 1.0 Hz led to improved agreement for both H<sub>1,6</sub> and H<sub>2,5</sub> signals. A direct comparison with the published spectrum at 60 MHz<sup>19</sup> was achieved by repeating the simulation using the optimized values of Table II, while resetting the frequency to 60 MHz; this resulted in much better agreement than using the previously published values (supplementary material, SM4).<sup>19</sup>

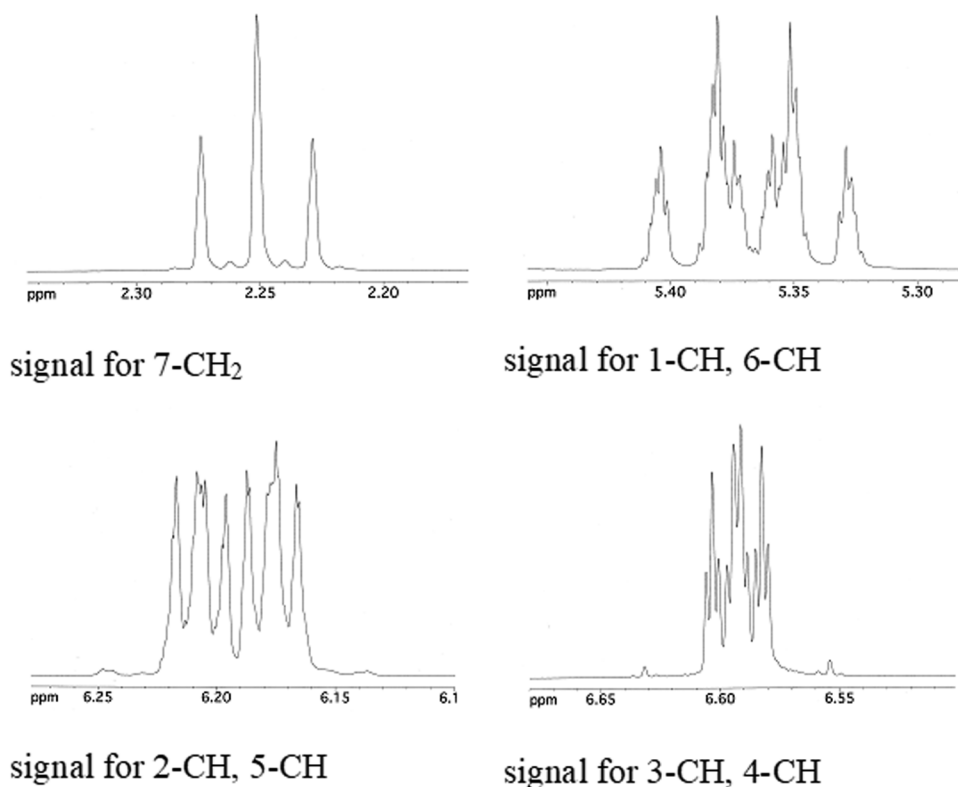


FIG. 2. Detailed form of the  $^1\text{H}$  NMR signals of CHT.

**TABLE II.** H–H Coupling constants as determined in this work compared with literature data.<sup>19,20</sup>

Coupling constant (Hz)	This work	Reference 19	Reference 20
${}^3J_{1-7} = {}^3J_{6-7}$	6.75	Not given	6.7
${}^3J_{1-2} = {}^3J_{5-6}$	9.0	8.58	8.9
${}^3J_{2-3} = {}^3J_{4-5}$	5.3	5.26	5.5
${}^3J_{3-4}$	10.8	10.67	11.2
${}^4J_{1-3} = {}^4J_{4-6}$	1.1	<sup>a</sup>	<sup>b</sup>
${}^4J_{2-4} = {}^4J_{3-5}$	0.8	0.8	0.7
${}^4J_{2-7} = {}^4J_{5-7}$	0.5	...	<0.4
${}^4J_{1-6}$	1.0	...	...
${}^5J_{1-4} = {}^5J_{3-6}$	0.5	<sup>a</sup>	<sup>b</sup>
${}^5J_{2-5}$	0.4	...	0.7 or –0.6
${}^5J_{1-5} = {}^5J_{2-6}$	...	...	...
${}^5J_{3-7} = {}^5J_{4-7}$	...	...	...

<sup>a</sup> $J_{1-3} + J_{1-4} = 1.56$  Hz.<sup>b</sup> $J_{1-3} + J_{1-4} = 1.5$  Hz.

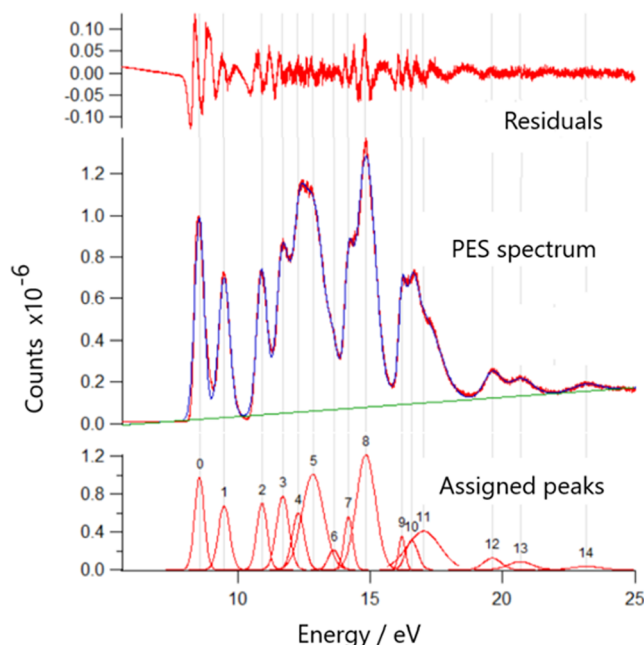
The non-equivalence of the 7-CH<sub>2</sub> protons in low-temperature NMR, and quantification of the energy associated with the fluxional process which renders them equivalent with increasing temperature, was the focus of the earliest studies.<sup>17,18</sup> We did not repeat these measurements.

## B. The photoelectron spectrum of CHT

This was obtained on the gas-phase line of the Elettra synchrotron (Basovizza, near Trieste, Italy) at room temperature, using previously described methods.<sup>1</sup> We used irradiation at both 30 eV and 55 eV. In each case, the data points (DPs) are separated by 0.005 eV (40 cm<sup>-1</sup>); those DPs (3875) in the 30 eV photon energy spectrum give a total resolution close to 8 meV. Those DPs in the 55 eV spectrum (7801) give a total resolution close to 23 meV. The analysis, by fitting 15 Gaussian peaks, as shown in Fig. 3, gives a close fit to the observed PES; the very low levels of residuals are shown in red. The fitted peak maxima, which we identify as the vertical ionization energies (VIEs), are listed in Table III. The adiabatic ionization energies (AIEs) were not determined from the observed PES since the onsets are not well-defined.

## C. Theoretical methods of structure determination

The GAUSSIAN-16 suite (G-16)<sup>29</sup> was used at the single configuration level for AIE determination of the first states of each symmetry. The most rigorous procedure was fourth order Møller-Plesset (MP4) perturbation theory, which was further enhanced by inclusion of single, double, and quadruple substitutions (MP4SDQ).<sup>30–33</sup> This method is energetically close to the coupled cluster (CC) method when singles, doubles, and selected triples [CCSD(T)] are included. This last procedure is widely accepted<sup>34–36</sup> as the gold-standard in quantum chemistry. The CCSD(T) computational cost formally scales as the seventh power of the size of the system, which can be prohibitive. Furthermore, CCSD(T) is more limited in G-16 and related suites than



**FIG. 3.** The photoelectron spectrum of CHT (in red). There is a close fit with the set of Gaussian functions (in blue), as shown in the assigned peaks. The residuals shown represent approximately 1% of the total count rate. The absolute positions of the assigned peaks are shown in Table III.

in MP4SDQ where the wave-functions (WFs) can be more widely utilized.

The multi-configuration self-consistent-field (MCSCF) modules in the MOLPRO suite<sup>37–39</sup> allow nomination of state symmetry and selection of the root of interest, which potentially enables determination of several AIE from either A' or A'' manifolds. However, seeking third or higher roots is frequently frustrated by potential energy curve crossings which can halt the determination; these occur widely during equilibrium structural searches. The MOLPRO version available to us is driven by relative energies within the state sequence, rather than eigenvector following, and is limited by this state switching. One route leading to higher roots which avoids this complication is to use the equilibrium structure of the (N – 1)th root as input to the following Nth root. When the two AIE are either well-separated in energy or structural nature, the surfaces generally show little interaction.

However, the initially unwanted curve crossing can lead to exciting and unexpected developments. When seeking the structure of the 1<sup>2</sup>A'' state, using either the X<sup>1</sup>A' or 1<sup>2</sup>A' structure as the starting point for the 1<sup>2</sup>A'' state, this led to a 1,6-interaction across the ring; the equilibrium structure of a norcaradiene cation was formed, as described below.

## D. Theoretical methods for analysis of the photoelectron spectrum

The PES, in Fig. 3, shows poorly defined AIE and an almost complete lack of vibrational structure. This legitimizes an alternative

**TABLE III.** Vertical ionization energies (eV) determined from the fit to the observed 30 eV spectrum in Fig. 3, together with one further peak from the 55 eV spectrum, where the area is not directly comparable. Fit errors in the last digit are in parentheses, while the fitting function parameters are shown. Total fitted points: 3875; total peak area:  $5.5411 \pm 0.073676$ ; and chi square: 2.061.

Peak position	Area	FWHM	FWHM sigma	Amplitude	Amp. sigma
8.56(1)	0.44(1)	0.4267(2)	0.002	0.971(4)	0.004
9.49(1)	0.36(1)	0.5041(3)	0.003	0.672(3)	0.003
10.92(1)	0.34(1)	0.4539(3)	0.003	0.700(4)	0.004
11.69(1)	0.37(2)	0.54(1)	0.01	0.65(3)	0.03
12.29(1)	0.11(2)	0.40(3)	0.03	0.26(4)	0.04
12.73(2)	1.418(6)	1.24(5)	0.05	1.06(1)	0.008
13.65(1)	0.05(8)	0.35(3)	0.03	0.12(1)	0.01
14.19(1)	0.21(1)	0.37(1)	0.005	0.54(1)	0.007
14.85(1)	1.09(1)	0.84(1)	0.004	1.21(1)	0.003
16.21(1)	0.10(1)	0.28(1)	0.008	0.35(1)	0.01
16.57(1)	0.18(1)	0.53(2)	0.02	0.31(8)	0.08
17.02(1)	0.63(1)	1.46(1)	0.01	0.41(1)	0.005
19.62(1)	0.10(1)	0.76(3)	0.03	0.12(1)	0.003
20.68(5)	0.096(1)	1.1	0.1	0.08(1)	0.003
23.18(5)	0.044(1)	1.2	0.1	0.03(1)	0.002
25.2(1)					

focus on vertical ionization energies (VIEs), which are performed using the  $X^1A'$  ground state equilibrium structure. A weakness is that neither the MCSCF method nor the MP4SDQ method gives VIE intensities. These intensities are more readily determined as pole strengths by using the Tamm–Dancoff approximation (TDA)<sup>41,42</sup> in GAMESS-UK.<sup>43</sup> The TDA suite is a single excitation configuration interaction (CIS) determination of ionic state energies for a nominated active molecular orbital (MO) set; the line intensities are given as pole strengths over a wide energy range. The electron propagator theory (EPT) in G-16, as the P3+ method of Ortiz,<sup>40</sup> is similar but is limited to outer-valence energies. The TDA method includes “shake-up” states (SU), where ionization is accompanied by electronic excitation.

The basis sets used were all triple-zeta in the valence shell with polarization (conventionally denoted TZVP),<sup>44–48</sup> including aug-cc-pVTZ, the Pople style 6-311G\*\*, and Karlsruhe default second series with additional p- and d-functions (def2-TZVPPD),<sup>47,48</sup> the choice varied with the numerical technique in progress.

### III. RESULTS AND DISCUSSION

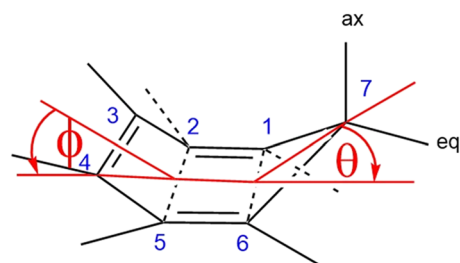
In this paper, the core MOs ( $4a' + 3a''$ ) are omitted, and valence shell numbering with occupied orbital sequence numbers 1–11a' and 1–7a'' is used throughout.

#### A. The ground state structure and the nature of the occupied MOs of CHT

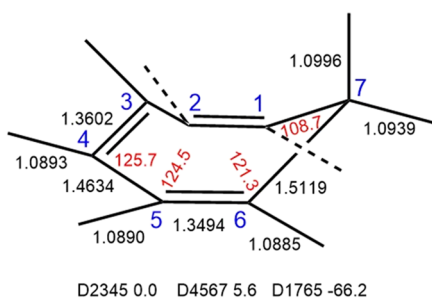
Structural studies for neutral CHT by microwave (MW) spectroscopy,<sup>49</sup> electron diffraction (ED),<sup>50</sup> and infrared spectroscopy<sup>51</sup> all support a  $C_s$  symmetry boat conformation, as shown in Fig. 4. This is conventionally represented by bow ( $\theta$ ) and stern ( $\phi$ ) angles from the central (planar) quartet of C-atoms. Although the molecule

is clearly exhibiting boat  $\rightleftharpoons$  boat conformational inversion, we find that the equilibrium structure is almost invariant with respect to the basis set or the theoretical method for equilibrium structure determination. Our complete MP4SDQ calculated structure is shown in Fig. 5; based on the rotational constants (RCs), it is closer to the MW<sup>49</sup> than the electron diffraction (ED) structure,<sup>50</sup> both of which made assumptions concerning some geometric parameters. Important dihedral angles are shown below the structure, which are in good agreement with previous studies.<sup>52–55</sup> The boat conformation local planes, relative to the central  $C_1C_2C_5C_6$  plane, have the 7-CH<sub>2</sub> group bow angle ( $\theta$ ) close to 35.6° and stern angle ( $\phi$ ) close to 52.9° for the  $C_2C_3=C_4C_5$  group.

The 7-H<sub>ax</sub> atom lies almost directly above the C<sub>7</sub> atom, and hence, its 1s-atomic orbital has a significant overlap with the C-atom  $\pi$ -orbital system, demonstrated in Fig. 6, by the electron density contours (at 0.02e) of the four highest occupied molecular orbital (HOMO) for the  $X^1A'$  state. A resemblance of the electronic



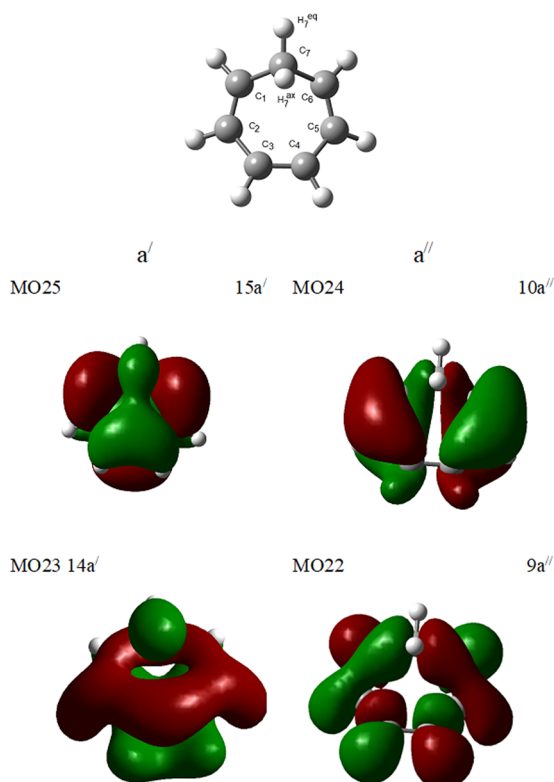
**FIG. 4.** The local planes which include the boat bow and stern angles ( $\phi$  and  $\theta$ ) for the  $C_2C_3=C_4C_5$  and 7-CH<sub>2</sub> groups relative to the central  $C_1C_2C_5C_6$  plane. H-atoms are not restricted to local CC=CC planes.



**FIG. 5.** The equilibrium structure of CHT from the MP4SDQ calculation, followed by anharmonic frequency determinations and correction for anharmonicity.

structure of CHT to benzene has been claimed.<sup>54</sup> The proximity of two symmetric  $\pi$ -bonds (MOs 23 and 25) together with the bow  $\text{CH}_2$  group leads to a major interaction.

We sought a transition state (TS) for the  $\text{CHT} \rightleftharpoons \text{NCD}$  neutral state isomerism, using the quadratic synchronous transit (QST2) procedure<sup>56,57</sup> in G-16. This TS, shown in the



**FIG. 6.** A ball and stick structure of CHT in the same conformation as the four highest occupied MOs of CHT below. The iso-electron density contours (0.02e) show a complex set of atomic orbital interactions. The shape of the HOMO  $15a'$  is very dependent on the bow and stern angles; where these are much higher, as in the  $1^2A'$  ionic state below, the structure is somewhat different (Fig. 7).

supplementary material as SM6, shows that the HOMO ( $15a'$ ) and HOMO-1 ( $10a''$ ) have exchanged positions in the energy sequence and that the CHT to NCD structure change has largely occurred in the TS, which lies 0.840 eV above the CHT ground state.

## B. The equilibrium structures of ionized CHT

### 1. The lowest ionic state ( $1^2A'$ )

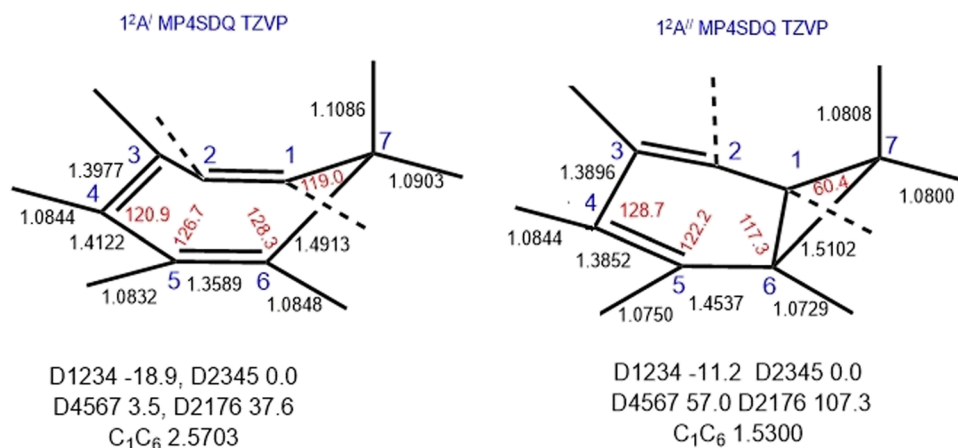
This is formed by one-electron ( $1e$ ) loss from the HOMO ( $15a'$ ) of CHT, as shown in Fig. 6. The ionic structure, with bow and stern angles ( $\phi$  and  $\theta$ )  $56.9^\circ$  and  $58.6^\circ$ , respectively, is much more compact than neutral CHT, showing that considerable electron density reorganization occurs on ionization. A comparison of MO  $15a'$  for the neutral molecule, in Fig. 6(a), with the ionic state is shown in the supplementary material as SM5. The lowest vibrational frequencies for the  $1^2A'$  state show one very low frequency mode; this leads to a high density of vibrational states in the lowest PES band. At the MP4SDQ level, the lowest frequencies are  $87$  ( $a'$ )  $\text{cm}^{-1}$ ,  $222$  ( $a''$ )  $\text{cm}^{-1}$ , and  $367$  ( $a'$ )  $\text{cm}^{-1}$ ; at the less rigorous Hartree-Fock level, the lowest frequency is even lower at  $51$   $\text{cm}^{-1}$ , with the higher frequencies virtually unchanged. These low values show that conformational inversion in the ionic state is more facile than the ground state. The relatively structureless PES is discussed further below.

### 2. The $1^2A''$ ionic state

Starting from the  $X^1A''$  state structure, the equilibrium structural search for the  $1^2A''$  state of CHT entails exchanging the orbital sequence of the HOMO ( $15a'$ ) and HOMO-1 ( $10a''$ ), which becomes the singly occupied MO (SOMO), at the outset and then locking the symmetry. However, we have found that for this state, using all basis sets and methods, during this optimization, the 7- $\text{CH}_2$  unit becomes more strongly tilted over the ring, with ( $\theta = 85^\circ$ ,  $\phi = 0^\circ$  at the MP4SDQ level). The interatomic distances  $\text{C}_1\text{C}_7$  1.5102 Å and  $\text{C}_1\text{C}_6$  1.5300 Å are similar, leading to the approximately equilateral triangular cyclopropane structure ( $\text{C}_1\text{C}_7\text{C}_6$ ), shown in Fig. 7; the overall structure is now **an ionic state of norcaradiene (NCD) and not the  $1^2A''$  state of CHT**. The vibrational frequencies of this NCD  $1^2A''$  state are all positive with lowest frequencies, 246 ( $a'$ ), 270 ( $a''$ ), and 368 ( $a'$ ). This shows a true minimum with a relatively rigid structure. The rotational constants (RCs; A, B, C) for both neutral and ionic states of CHT show nearly degenerate values for A and B. The  $X^1A'$  state in Fig. 5 has A, B, and C: 3682.59 MHz, 3639.09 MHz, and 2018.29 MHz, while the ionic structures in Fig. 7 give values 3525.62 MHz, 3466.84 MHz, and 1779.08 MHz ( $1^2A'$ , CHT). Those for NCD ( $1^2A''$  state) are 4491.17 MHz, 3305.51 MHz, and 2217.67 MHz, respectively. Thus, tilting of the  $\text{CH}_2$  unit can easily be followed through changes in these RCs as the equilibrium structure search  $\text{CHT} \rightarrow \text{NCD}^+$  proceeds. In the absence of a graphical user interface (GUI), this RC approach could be generally important for studying isomerism changes.

### 3. The structural process $\text{CHT} \rightarrow \text{NCD}$ in the cationic states

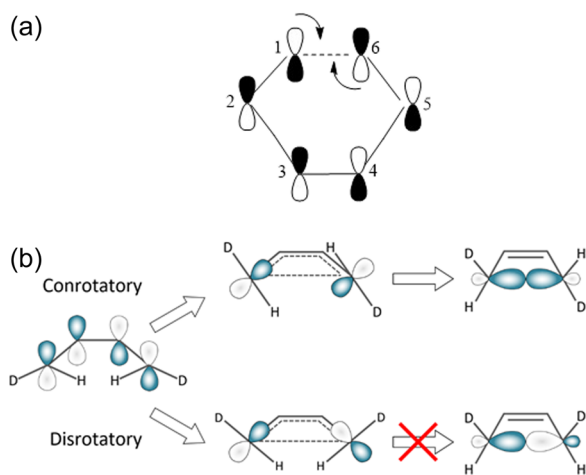
This is an example of an electrocyclic reaction, the concerted cyclization of a conjugated  $\pi$ -electron system by converting



**FIG. 7.** The first two adiabatic ionization energy structures determined at the MP4SDQ level are fundamentally different, with  $1^2A'$  a CHT cation, while  $1^2A''$  is an NCD structure.

one  $\pi$ -bond to a ring forming  $\sigma$ -bond. When a photochemical ring closure is affected, the stereospecificity is opposite to that of a thermal ring closure.<sup>58,59</sup> A related example is *trans, cis, trans*-2,4,6-octatriene, which undergoes a thermal ring closure to *cis*-5,6-dimethyl-1,3-cyclohexadiene (DMCH); the photochemical ring closure gives the *trans*-DMCH.<sup>60</sup>

As expected for a  $1^2A''$  state, the SOMO is nodal through the 7-CH<sub>2</sub> group, as shown in Figs. 6 and 8. During the structural change, the 7-CH<sub>2</sub> unit of CHT<sup>+</sup> bends upward and over the ring, leading to a tilt of the H-C<sub>1</sub> and H-C<sub>6</sub> bonds outward.



**FIG. 8.** (a) The conrotatory motion leading to conversion of the  $1^2A''$  cycloheptatriene cation to the one based on norcaradiene, where a new  $C_1C_6$  bond is formed; the arrows show the local atomic and orbital movement, which generates the new  $\sigma$ -bond. (b) The general procedure for conrotatory processes shown here, contrasting with the forbidden disrotatory process, where an anti-bonding result is obtained.

The 7-CH<sub>2</sub> group has been omitted in Fig. 8 since it leads to a congested diagram. Conrotatory motion of these H-C<sub>1</sub> and H-C<sub>6</sub> groups, shown by the curved arrows, forms the new  $C_1C_6$  bond. This is then accompanied by (or followed by) further electronic rearrangement since the bulk of the cationic charge lies in the new 6-membered ring rather than the 3-membered one. This ionic state correlation using two centers of the singly occupied MO follows the known<sup>58,59</sup> conrotatory behavior in many photochemical reactions where  $(4n + 2)$  electrons are involved. Here, the three alkene bonds provide 6-electrons, with  $n = 1$ , since the potentially additional  $2e$  from the 7-CH<sub>2</sub> group is not involved.

An immediate implication is that the study on the CHT PES assignment must be performed using vertical theoretical studies, as done in Sec. III D, and that a comparison with the predicted PES of NCD becomes important. We conclude that there is little barrier to formation of an NCD cation from the  $1^2A''$  state of CHT.

#### 4. The search for CHT cations of $2^2A''$ symmetry

This was performed to determine whether  $1^2A''$  states of CHT exist as energy minima. Structures and AIE for both  $2^2A'$  and  $2^2A''$  states from MCSCF wave-functions (WFs) using the MOLPRO suite proved good starting points, with the results shown in Table IV. Only the occupancy of the six highest doubly occupied molecular orbitals (DOMO) of the ground state ( $3a' + 3a''$ ) followed by the two lowest unoccupied molecular (virtual) orbitals (LUMOs) of each symmetry is shown. In MCSCF calculations, difficulty in balancing the number of configurations in the ground state with many more in the ionic states always leads to low values for AIE, here by  $\sim 1$  eV. In some cases, the WF showed two leading configurations; in our experience, symmetric and antisymmetric combinations of configurations frequently occur in MCSCF calculations but are absent in multi-reference multi-root configuration interaction (MRD-CI) and other multi-configuration methods. This may be a result of the limited active set of MOs, an essential prerequisite in MCSCF studies, to control the calculation dimensions. This contrasts with MRD-CI,



**TABLE IV.** MCSCF adiabatic ionization energies for CHT assuming  $C_s$  symmetry; using 26 460 determinants with 11 electrons permuted into 10 orbitals ([11,10]-singles and doubles excitation MCSCF).

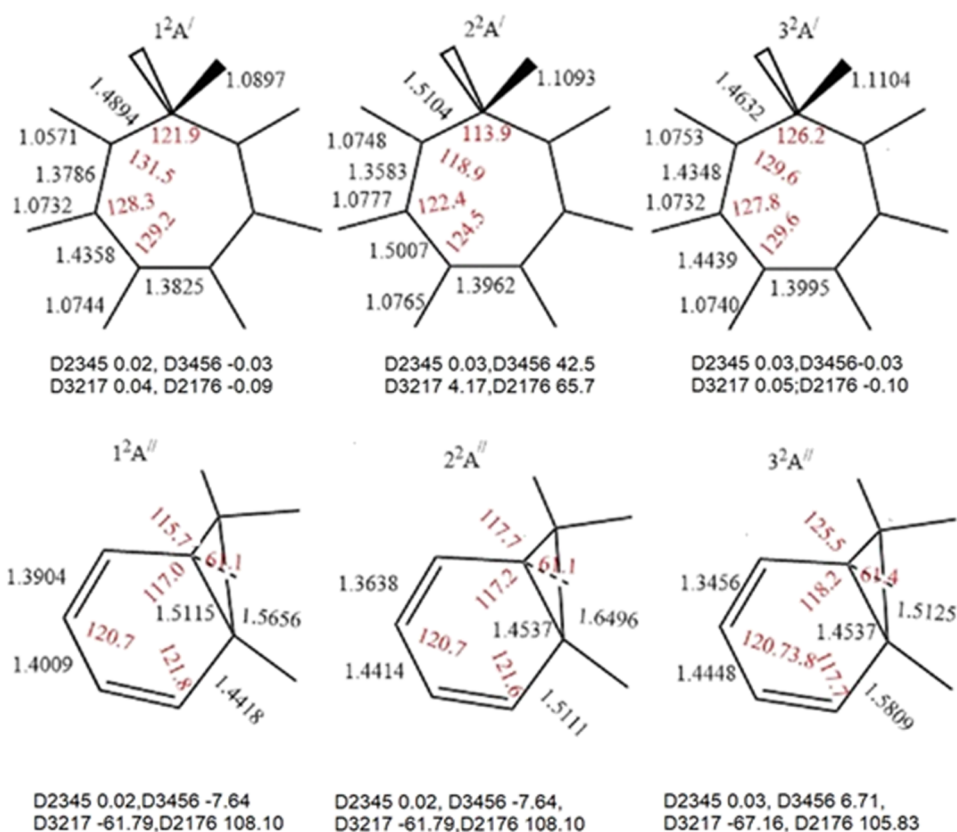
State	AIE (eV)	Active MO leading configuration ( $a'$ ; $a''$ )	CI eigenvector	Structure
$X^1A'$	0.0000 <sup>a</sup>	22 200; 22 200	0.9630	CHT
$1^2A'$	7.5219	22a00; 22 200	0.9470	CHT
$1^2A''$	7.7280	22 200; 22a00	0.9546	NCD
$1^2A''$	8.1829	22 200; 22a00	0.8141	CHT
$2^2A'$	10.7316	2a200; 22 200 220a0; 22 200	0.7345–0.3784	CHT
$2^2A''$	10.7516	22 200; 2a200 22 220; 2a000	0.8868–0.1749	NCD
$2^2A''$	10.5229	22 200; 2a200 22 200; 22a00	0.7448 +0.3100	CHT
$3^2A'$	12.1852	2a200; 22 200 220a0; 22 200	0.4083–0.5250	CHT
$3^2A''$	12.4496	22 200; a2200	0.9212	NCD

<sup>a</sup>MCSCF energy  $X^1A'$  state –269.843 37 a.u.

where we usually include all valence shell DOMOs and virtual orbitals.<sup>2</sup>

In all cases, the cationic MCSCF results in Table IV paralleled the MP4SDQ studies above, for the first state of each symmetry.

The MCSCF structures, shown in Fig. 9, present wide structural variation. Both the  $1^2A'$  and  $3^2A'$  states are effectively planar and hence of  $C_{2v}$  symmetry. The  $2^2A'$  state retains the CHT connectivity and is non-planar. All three of the  $1^2A''$  to  $3^2A''$  states show NCD

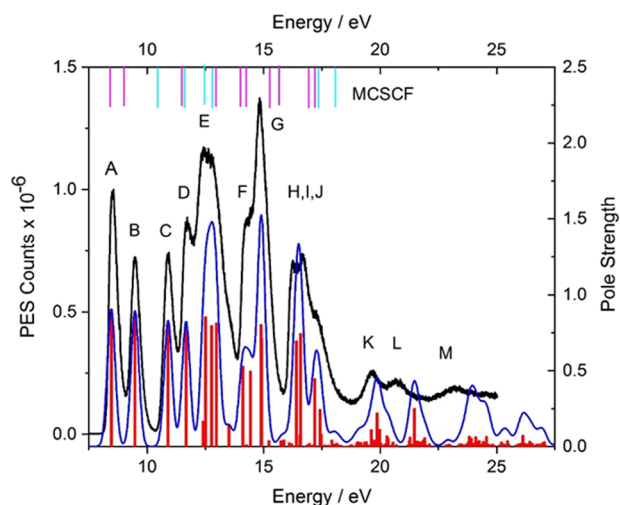
**FIG. 9.** The MCSCF cationic states of CHT and NCD at equilibrium. These start the equilibrium structural search for the ionic state from the  $X^1A'$  state structure.

structures, when the equilibrium structure searches start from an initial  $X^1A'$  geometry as above.

At this point, it appeared that a wide scan of the CHT/NCD surface for the  $X^2A''$  state of CHT was necessary. Starting from the  $X^1A'$  ground state, we used a z-matrix with dummy atoms along the  $C_s$  symmetry axis. Two torsion angle parameters, representing each of the non-planar units attached to the central planar  $C_1C_2C_5C_6$  unit, were systematically varied using the G-16 “scan” provision. Over one hundred data points obtained showed systematic changes, as shown as a 3D-plot in the [supplementary material](#) as SM13. Plotting the sequence of points against energy gave a more informative result as shown in the [supplementary material](#), SM14. All the local minima in SM14 correspond to the dihedrals being close to the equilibrium structure ones, and all showed NCD structural features, through the presence of an apparent cyclopropane moiety. Initially, we concluded from this that there is no evidence of stable CHT  $X^2A''$  states. However, this was later shown to arise from the chosen non-bonded distances between  $C_1$  and  $C_6$  being too close; this is investigated further in Secs. III F and III G.

### C. Assignment of the wide scan CHT photoelectron spectrum

The full spectrum, where the individual bands are labeled A to M, is shown in Fig. 10. The results of the theoretical Tamm–Dancoff approximation (TDA)<sup>41,42</sup> energies and intensities are superimposed on the base-line. The vertical approximation ionic states determined by MCSCF, shown in Fig. 10, have color differentiation as  $^2A'$  (magenta) and  $^2A''$  (cyan) states. The TDA pole strengths, shown as



**FIG. 10.** The wide scan photoelectron spectrum collected at 55 eV. There is a close comparison between the 30 eV and 55 eV PES kinetic energy spectra. An assignment using the Tamm–Dancoff approximation is shown with pole strengths (in red). The overall spectral profile based on the TDA procedure is shown (in blue), using a set of Gaussian functions with a full width at half height of  $3200\text{ cm}^{-1}$ . MCSCF ionic state VIEs, shown at the top, have color differentiation for  $^2A'$  (magenta) and  $^2A''$  (cyan) states.

red vertical bars, are summed in blue by a gaussian function, where the line width was chosen to fit the width of the lowest ionization peak. The wide range TDA energy results ( $E_{\text{TDA}}$ ) are based on a linear fit to the energies to the PES values using the relationship  $\text{VIE} = 0.9E_{\text{TDA}} + 1.20\text{ eV}$ . This enables the two sets of energies to show close correlation up to about 17 eV; a quadratic function would be required to force a closer correspondence in the  $C_{2s}$  region above 20 eV. The TDA energy values are correlated with the PES maxima in Table V.

All the present theoretical methods predict the lowest AIE to be  $1^2A'$ . Since it appears that the  $1^2A''$  state undergoes structural change to an NCD cation, the energy differences between these two states at equilibrium, 1.368 eV (MP2) or 0.481 eV (MP4SDQ), cannot be related to the PES band separation.

**TABLE V.** The TDA assignment of the overall photoelectron spectrum. The peaks are labeled with the deconvolution shown in Fig. 3. The lowest shake-up states occur at 12.406 eV ( $A''$ ) and 13.508 eV ( $A'$ ).

PES peak	Vertical IE (eV)	Attribution	TDA assignment <sup>a</sup>		
			State	VIE (eV) <sup>b</sup>	Pole strength <sup>c</sup>
P0	8.55 ; 0.01	A	$1^2A'$	8.458	0.906
P1	9.49 ; 0.01	B	$1^2A''$	9.476	0.894
P2	10.91 ; 0.01	C	$2^2A'$	10.899	0.830
P3	11.66 ; 0.05	D	$2^2A''$	11.670	0.824
P4	12.25 ; 0.03	E	$3^2A''$	12.406	0.165
			$3^2A'$	12.502	0.856
			$4^2A'$	12.761	0.797
P5	12.84 ; 0.01	E	$4^2A''$	12.966	0.814
			$5^2A'$	13.508	0.140
			$6^2A'$	14.101	0.530
P6	13.62 ; 0.01	F	$7^2A'$	14.430	0.497
			$3^2A''$	14.884	0.804
			$8^2A'$	14.914	0.710
P7	14.16 ; 0.02	F	$2^2A''$	16.555	0.074
P8	14.83 ; 0.02	G	$2^2A'$	16.584	0.746
			$2^2A'$	17.200	0.448
			$2^2A'$	17.420	0.244
P9	16.19 ; 0.01	H	$2^2A'$	17.468	0.078
			$2^2A''$	17.627	0.111
			$2^2A''$	18.872	0.221
			$2^2A''$	19.979	0.113
P10	16.58 ; 0.02	I	$2^2A''$	20.294	0.070
			$2^2A'$	21.469	0.252
			$2^2A''$	23.890	0.029
P11	17.2 ; 0.1	J	$2^2A''$	23.916	0.023
			$2^2A''$	23.916	0.023
			$2^2A''$	23.916	0.023
P12	19.63 ; 0.02	K	$2^2A''$	19.627	0.111
			$2^2A''$	19.872	0.221
			$2^2A''$	19.979	0.113
P13	20.69 ; 0.02	L	$2^2A''$	20.294	0.070
			$2^2A'$	21.469	0.252
			$2^2A''$	23.890	0.029
P14	23.2 ; 0.1	M	$2^2A''$	23.890	0.029
			$2^2A''$	23.916	0.023
P15	25.2 ; 0.1	M	$2^2A''$	23.916	0.023

<sup>a</sup>A Greens's function (GF) all-valence CIS study gave VIE for the four lowest roots: 8.3465( $1^2A'$ ), 9.694( $1^2A''$ ), 11.772( $2^2A'$ ), and 12.994 eV( $2^2A''$ ).

<sup>b</sup>An all-valence electron MRD-CI study gave VIE for the four lowest roots: 7.861( $1^2A'$ ), 8.762( $1^2A''$ ), 8.999 ( $2^2A'$ ), and 9.184 eV ( $2^2A''$ ).

<sup>c</sup>The EPT suite in G-16, equivalent to outer-valence Greens's function (OVGF) +P3, gave the AIE sequence: 7.399 ( $1^2A'$ ), 9.898( $1^2A''$ ), 11.117( $2^2A'$ ), and 11.635 eV( $2^2A''$ ), respectively.

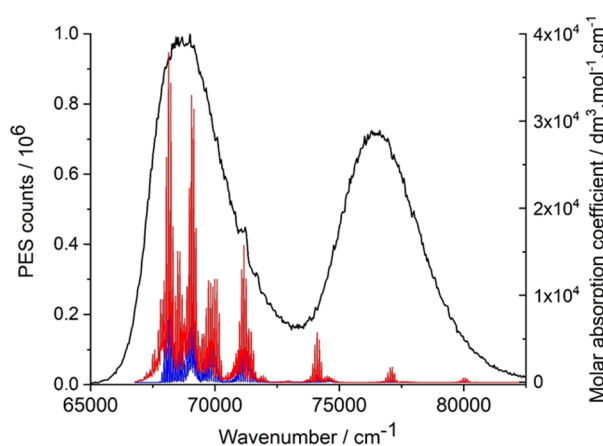
We believe that the overall AIE sequence for CHT is  $1^2A' < 1^2A'' < 2^2A' < 2^2A''$  and is a reliable interpretation of the low-lying VIE. This is further supported by several less sophisticated methods. Three footnotes to Table V show the first four VIEs determined by other theoretical methods. Greens's Function (GF) calculation, shown in footnote "a," is a further CIS procedure, closely related to the TDA method. Footnote "b" shows the electron propagator theory (EPT) method, including outer valence Greens's Function (OVGF) and electron propagator theory (P3).<sup>40</sup> Footnote "c" shows the results of an all-valence electron MRD-CI study,<sup>43</sup> limited to just the four lowest VIEs. The absolute values differ, but the symmetry sequence is identical in all these methods, which leads us to assign symmetries of the leading states in the experimental spectrum with confidence.

#### D. Comments on the lack of vibrational structure in the PES

The present spectrum in Fig. 10 shows a much higher signal-to-noise ratio than other previous studies,<sup>3,5-7</sup> but none of the PES bands show well developed vibrational structure. The band A onset (AIE) of the spectrum is probably below 8.00 eV, with its maximum (VIE) near 8.55(1) eV. Traeger *et al.*<sup>4</sup> found the AIE of CHT to be rather higher than is observed here, 8.29 eV, by using a photoionization efficiency (PIE) procedure; but their VIE agrees with the present study. A sigmoid fit to the leading edge of band A discloses an irregular series of local peaks. The most frequent interval, showing a separation of 80  $\text{cm}^{-1}$ , is close to the lowest frequency for the calculated  $1^2A'$  state (87  $\text{cm}^{-1}$ ) at the MP4SDQ level.

#### E. Assignment of the PES using the theoretical vibrational structure of the lowest ionic states, $2^2A'$ and $2^2A''$

Using the MP4SDQ vibrational wave-function, the predicted envelope of the lowest ionic state (band A) is shown in Fig. 11,



**FIG. 11.** The lowest two ionization potentials of CHT, with the Franck-Condon profile of the vibrational structure superimposed. The stick structure shows both the cold band (blue) and the combined hot and cold band (red) structure. The Half-Width at Half-Maximum (HWHM) is 10  $\text{cm}^{-1}$  for the states shown.

**TABLE VI.** The lowest vibrational states with their intensities and assignments for the  $2^2A'$  state, at the MP4SDQ level. The 0-0 transition was 65 834  $\text{cm}^{-1}$ . The labeling of states follows an increasing sequence in frequency. Mode 1 is the lowest frequency, while the number of quanta is given as superscripts ( $1^3$  means 3 quanta of mode 1, etc.).

Vibrational state ( $\text{cm}^{-1}$ )	Vibration and quanta	Intensity
0	0	123
88	$1^1$	790
175	$1^2$	3477
263	$1^3$	8733
350	$1^4$	13 520
438	$1^5$	12 820
455	$3^1; 1^1$	208
525	$1^6$	6621
543	$3^1; 1^2$	995
613	$1^7$	1134
630	$3^1; 1^3$	2746
667	$4^1; 1^3$	299
718	$3^1; 1^4$	4751
754	$4^1; 1^4$	322
788	$1^9$	751
794	$2^2; 1^4$	253
805	$3^1; 1^5$	5178
818	$7^1; 1^2$	405
875	$1^{10}$	504
882	$2^2; 1^5$	234
893	$3^1; 1^6$	3291
906	$7^1; 1^3$	1045
980	$3^1; 1^7$	904
993	$7^1; 1^4$	1683
998	$3^2; 1^3$	201
1005	$10^1; 1^2$	817
1020	$12^1; 1^1$	713
1055	$9^1; 1^3$	398
1081	$7^1; 1^5$	1693
1085	$3^2; 1^4$	423
1093	$10^1; 1^3$	2653
1108	$12^1; 1^2$	3208
1134	$14^1; 1^2$	228
1142	$9^1; 1^4$	724
1155	$3^1; 1^9$	221
1168	$7^1; 1^6$	972
1173	$3^2; 1^5$	576
1180	$10^1; 1^4$	5410
1195	$12^1; 1^3$	8294
1222	$14^1; 1^3$	602
1230	$9^1; 1^5$	835
1240	$15^1; 1^3$	332
1243	$3^1; 1^{10}$	267
1256	$7^1; 1^7$	145

TABLE VII. The  ${}^2A'$  state frequencies as used in the Franck–Condon analyses.

$A'$	88	$A'$	959	$A'$	1495
$A''$	222	$A'$	977	$A''$	1527
$A'$	367	$A''$	1008	$A''$	1572
$A'$	404	$A''$	1036	$A'$	1608
$A''$	419	$A'$	1092	$A'$	1671
$A''$	483	$A''$	1152	$A'$	2940
$A'$	643	$A''$	1245	$A'$	3141
$A''$	783	$A'$	1265	$A''$	3211
$A'$	792	$A''$	1300	$A'$	3217
$A'$	830	$A'$	1318	$A''$	3219
$A''$	876	$A''$	1441	$A'$	3227
$A'$	933	$A'$	1442	$A''$	3239
$A''$	943	$A''$	1457	$A'$	3240

TABLE VIII. The  ${}^2A''$  state frequencies as used in the Franck–Condon analyses.

$A'$	184	$A'$	1008	$A''$	1556
$A'$	249	$A'$	1100	$A'$	1597
$A''$	418	$A''$	1120	$A'$	1615
$A''$	467	$A'$	1120	$A''$	1655
$A''$	565	$A''$	1157	$A'$	1713
$A'$	609	$A''$	1164	$A''$	3283
$A'$	798	$A'$	1201	$A'$	3286
$A''$	810	$A''$	1233	$A'$	3295
$A'$	835	$A''$	1270	$A''$	3338
$A''$	897	$A'$	1292	$A'$	3342
$A'$	904	$A'$	1332	$A''$	3358
$A''$	920	$A''$	1481	$A'$	3369
$A''$	1000	$A'$	1519	$A'$	3400

with the lowest vibrational states in Tables VI, VII and VIII. The dominance of low frequency states is apparent. The near absence of states where the highest frequencies are involved leads to almost all calculated vibrational structure lying under the lowest IE. The lack of vibrational structure in the observed present PES can be readily attributed to the high density of states; the  $C_S \rightleftharpoons C_S$  inversion may well lead to further line broadening. A summary of some of the major contributors to the vibrational structure is shown in Table V. The hot band structure although important in Fig. 11 is made up of a multiplicity of weak bands none of which have significant intensity; the actual onset lies  $1008\text{ cm}^{-1}$  below the 0-0 band. The residuals of  $IE_1$  under  $IE_2$  would necessitate special techniques to distinguish them from the main  $IE_2$  structure. Single vibrational states will have a Half-Width at Half-Maximum (HWHM) close to  $70\text{ cm}^{-1}$  in our experience. The present calculated values will cover the main part of the  $IE_1$  envelope, with a HWHM of close to  $400\text{ cm}^{-1}$ ; such a value was previously found appropriate when there was interaction with a nearby ionization.

A similar situation occurs with the band B centered near  $76400\text{ cm}^{-1}$ . The lowest calculated  $X^2A''$  ionic state has lowest frequency  $184\text{ cm}^{-1}$ , as shown in Table VIII. The fit of the cold band data, shown in Table VIII, is in Fig. 12. Most of the cold band vibrational intensity is composed of low frequency vibrations, as with band A. The loss of experimental vibrational structure arises from the same result, a high density of vibrational states, where low frequencies dominate. G-16 attributes this to an NCD rather than a CHT structure; this is discussed further in Sec. III F.

## F. Investigation of the nature of the bonding in the $X^2A''$ state

In this section, we determine whether bonds exist between formally non-bonded atoms; for example, CHT does not have a bond between  $C_1$  and  $C_6$ , whereas NCD has a normal  $C_1C_6$   $\sigma$ -bond. Using the “Atoms in Molecules” (AIM) approach of Bader *et al.*, as implemented in the Quantum Theory of Atoms in Molecules (QTAIM)

software,<sup>61–64</sup> we determine the “critical points (CPs)” where the gradient of the electron density along each internuclear distance is zero. A plot of the critical points (CPs) for CHT in its  $X^1A'$ ,  $X^2A'$ , and  $X^2A''$  states, and the NCD  $X^1A'$  state, is shown in Figs. 13(a)–13(d). For each electronic state, the CPs are in red, with the background atomic skeleton in black. CPs occur between all bonded pairs of atoms and the center of each ring. Thus, for the CHT  $X^1A'$  state [Fig. 13(a)], there are a total of 16 CP, which include one for the 7-membered ring center but crucially not between  $C_1$  and  $C_6$ . NCD [Fig. 13(b)] has CP such as the CHT set, but in addition, it has CP for both the  $C_1C_6$ -bond and the cyclopropane ring. The  $X^2A'$  state [Fig. 13(c)] of CHT behaves the same as the  $X^1A'$  neutral state. The primary state of interest is the  $X^2A''$  state, which may be either of CHT or NCD type of structure. It shows, in Fig. 13(d), the NCD group, including the cyclopropane ring and  $C_1C_6$  CPs. Thus, at equilibrium, the  ${}^2A''$  state is clearly of the NCD type. These inter-nuclear CP separations from the atoms define atomic

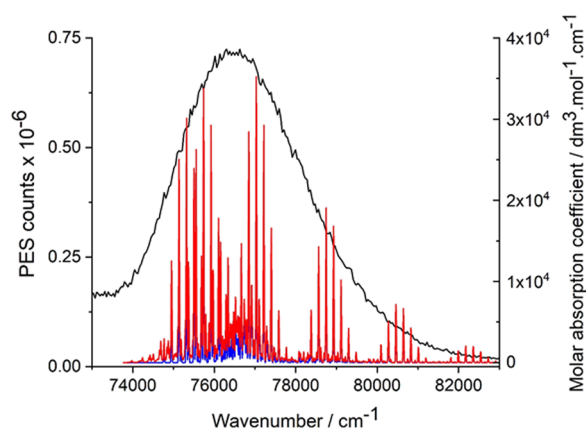
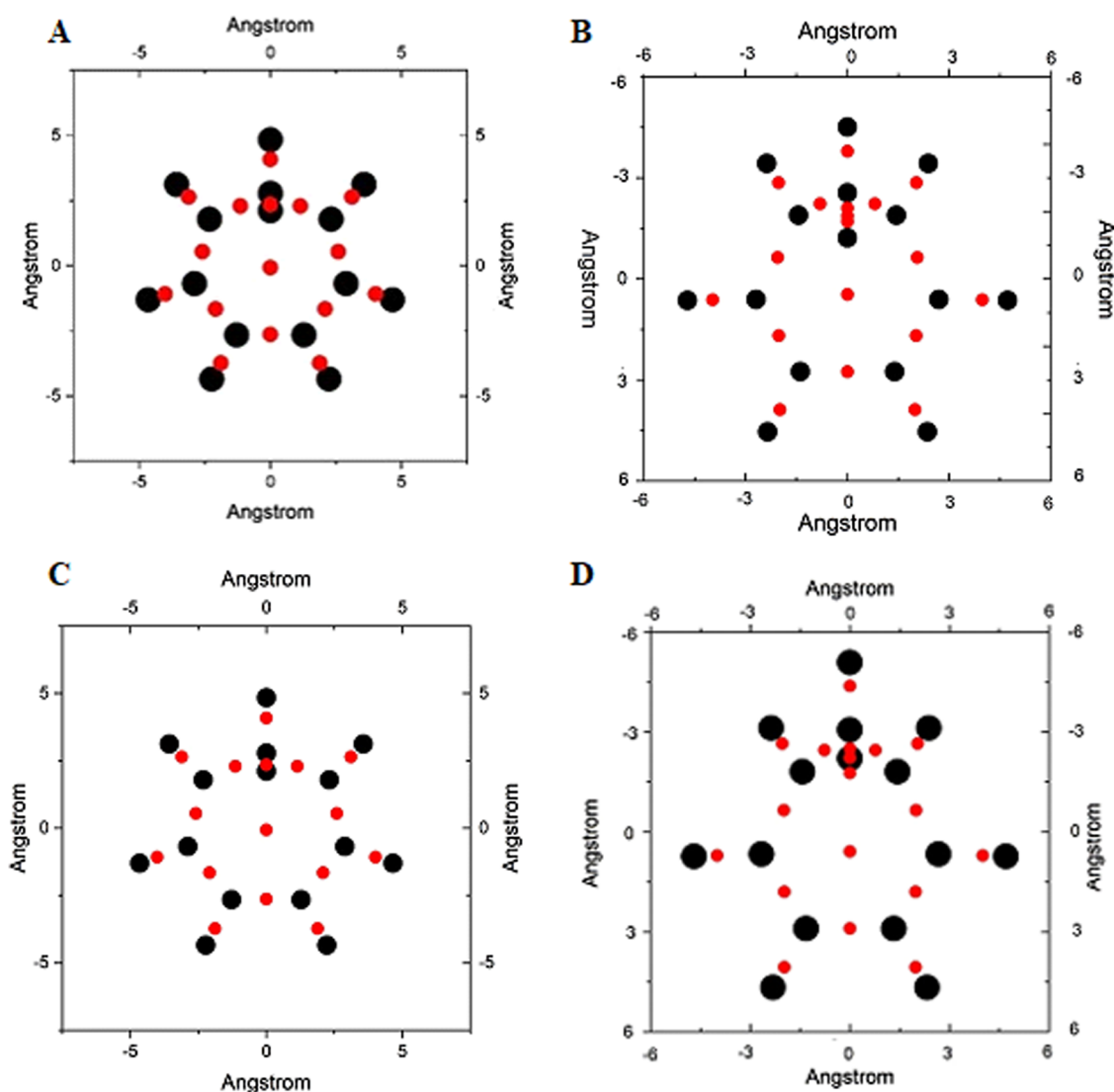


FIG. 12. The second lowest ionization potential (Band B) of CHT, with the Franck–Condon profile of the vibrational structure superimposed. The stick structure shows both the cold band (blue) and summation with the hot band structure (red). The Half-Width at Half-Maximum (HWHM) is  $10\text{ cm}^{-1}$  for the states shown.



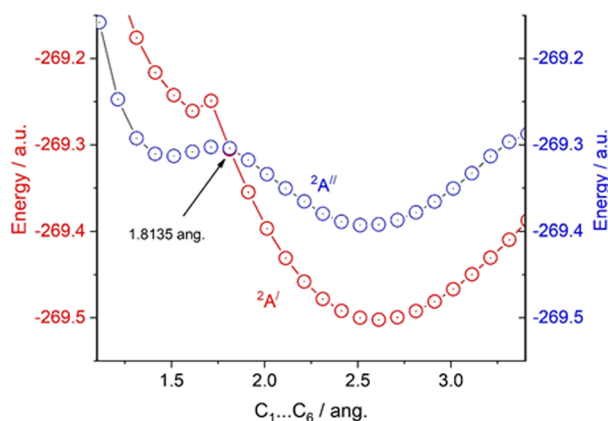
**FIG. 13.** The bond and ring critical points for CHT, NCD,  ${}^2A'$  state of CHT and  ${}^2A''$  state of CHT (actually an NCD). CPs which occur at all atomic nuclei have been omitted for simplicity.

basins; the electron density within these basins generates the integrated electron density. The bond CPs lie closer to the H-atoms than the C-atoms and thereby give a measure of the local bond dipoles.

When the vertical state  $X^2A''$  of CHT is used in the QTAIM package,<sup>61–64</sup> the number and positions of the CP are like those for both the  $X^1A'$  and  $X^2A'$  states, showing that these are CHT rather than NCD states. Thus, the formation of the *adiabatic* NCD cation is a result of the proximity of the  $C_1$  and  $C_6$  atoms and the ability for conrotatory interaction in the SOMO of the state leading to the NCD structure. None of the  $A''$  MOs of this vertical  ${}^2A''$  state show evidence of  $C_1C_6$  bonding.

### C. The energy surfaces and structures of the CHT and NCD cations as a function of the $C_1$ to $C_6$ distance

A plot of these surfaces using a  $C_S$  symmetry z-matrix is shown in Fig. 14. The curves for the two states, red ( ${}^2A'$ ) and blue ( ${}^2A''$ ), show a crossing at a  $C_1C_6$  distance of 1.8135 Å. The curve crossing  $C_1C_6$  length in the  ${}^2A'$  states is substantially larger than that for NCD (shown in Fig. 7) and smaller than that for CHT (2.6155 Å). However, both symmetry states show two minima, and this confirms that  ${}^2A''$  cationic states of CHT *do have equilibrium structures*; the key point is that the optimization must be performed with a large



**FIG. 14.** A study of the energy surfaces under  $C_S$  symmetry, for the  ${}^2A'$  (in red) and  ${}^2A''$  (in blue) states, as a function of the  $C_1$  to  $C_6$  separation. The difference in state symmetry allows the curve crossing shown. Two minima occur for each state, which correspond to NCD (at short  $C_1C_6$  distance) and CHT (at long distance). These clearly show the existence of  ${}^2A''$  states for CHT. This shows the need to scan a wide range of interatomic distances in such cases and that starting near the equilibrium structure of the neutral ground state can lead to misleading results.

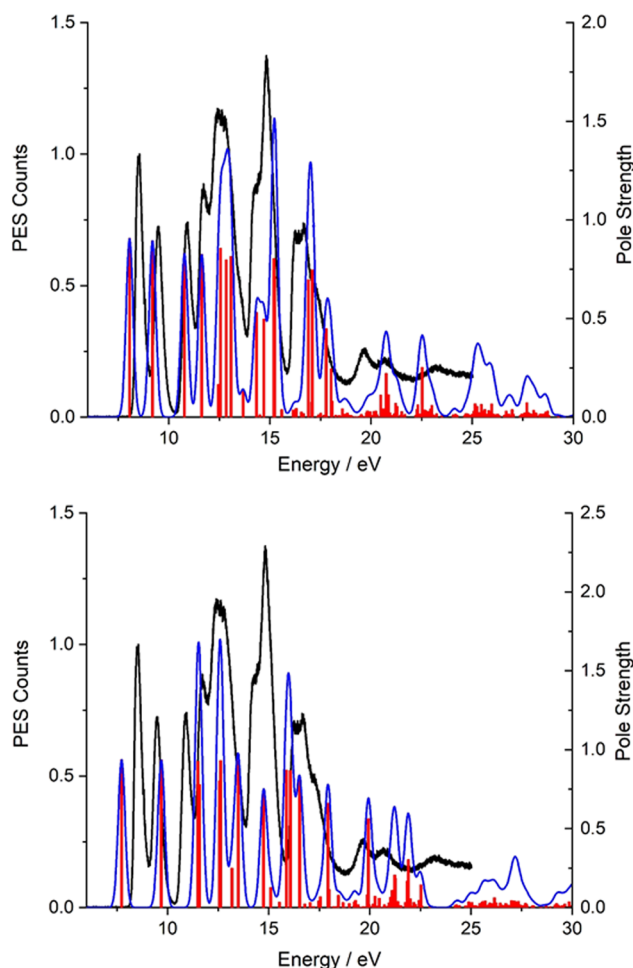
$C_1C_6$  distance to succeed; otherwise, only NCD states are formed. The switch of symmetry in the two leading ionic states for NCD relative to CHT was noted in the QST2 procedure used for the neutral compound transition state above.

At the two extrema for the  $C_1C_6$  distance in Fig. 14, the structures are still basically CHT ( $>3.25$  Å) and NCD (1.25 Å). At the crossover, the  $C_1C_2/C_5C_6$  distances are lengthened, while those between centers  $C_2C_3C_4C_5$  are shortened. For all  $C_1C_6$  distances larger than at the crossover, the  ${}^2A'$  and  ${}^2A''$  states are both planar. At its minimum, the  ${}^2A''$  state has  $C_1C_2$ ,  $C_2C_3$ ,  $C_3C_4$ , and  $C_1C_7$  bonds 1.3750 Å, 1.4809 Å, 1.3152 Å, and 1.4896 Å, respectively; these are more strongly alternating than in the  ${}^2A'$  state.

An avoided crossing between these two states can be obtained by performing the surface calculation with  $C_1$  symmetry in the z-matrix. The resulting curve (supplementary material as SM13) is very similar to that in Fig. 14, except that the lower energy  ${}^2A_1$  state at large  $C_1C_6$  distances continues with the lower energy  ${}^2A''$  blue state at short distances.

## H. The predicted photoelectron spectrum of norcaradiene

As a final check that the observed PES from the CHT sample is, indeed, the PES of CHT and not that of NCD, we show a direct comparison of these two theoretical spectra in Fig. 15. In the absence of a direct comparison between theory and experiment for NCD, we show unscaled energies for both calculations. Thus, the theoretical energy scale for CHT differs from that shown in Fig. 10. The gaussian line widths used have a full width at half height (FWHM) of  $3200\text{ cm}^{-1}$ . As expected, the two theoretical spectra show some similarity, owing to the number of shared types of bonds in a similar structural environment. Critically, the two theoretical spectra differ significantly in the



**FIG. 15.** A direct comparison of the theoretical ionization spectra of NCD (bottom) and CHT (top) at the TDA level. There is clearly a closer match between the PES and CHT results.

low energy region. There seems little doubt that the CHT input sample does generate the PES of CHT and not NCD under the current conditions.

## IV. CONCLUSIONS

At the outset of this study on the PES of CHT, we did anticipate a necessity for the consideration of the potential energy relationships between CHT and NCD. Although the two isomers had previously been shown to interchange in some reactions, early studies on the  ${}^1\text{H}$  and  ${}^{13}\text{C}$  NMR spectra of CHT appeared to be unambiguous concerning the nature of the sample input to the PES experiment. The current NMR spectra shown here confirmed this view. Our spectra employed spin tickling and 2D-NMR techniques, not available to the earlier  ${}^1\text{H}$  and  ${}^{13}\text{C}$  studies. As a result, our new analyses identified several different coupling constant values; these reproduce the lower frequency spectra as well and, hence, should replace previous values.

When the equilibrium structures for the ionic states of CHT were sought, only those of  ${}^2A'$  symmetry had rotational constants consistent with the CHT skeleton. It became apparent that all attempts to generate  ${}^2A''$  structures of CHT in fact led to NCD cations. This was proved by our 3-dimensional “scan” of the potential energy surface for  ${}^2A''$  states as the CHT structure was varied. However,  ${}^2A''$  states *do exist* for both CHT and NCD, but these have limited ranges of the  $C_1C_6$  distance. The proximity of the  $C_1C_2$  and  $C_5C_6$  alkene bonds appears to be the driving force for cross-ring interactions in a classic case of conrotatory interaction of the SOMO forming the  $C_1-C_6$  bond. This is consistent with the widespread view that thermal and photochemical processes use opposite rotations of the HOMO; the ionic states follow the photochemical route. The potential energy surfaces for the two lowest states cross under  $C_5$  symmetry, which is avoided by performing the calculations under  $C_1$  symmetry.

Under the QTAIM analysis, the  $X^1A'$  ground state and  $X^2A'$  lowest ionic state show critical points consistent with the CHT nucleus. Indeed, when the QTAIM is performed on the vertical structure of the  $X^2A''$  state, this also exhibits a CHT pattern. However, all attempts to generate an equilibrium structure for the  $X^2A''$  state always led to NCD cations with their differing numbers of CP.

The question remained as to whether the observed PES was that of CHT or NCD. In fact, the PES of NCD has been claimed by Bieri *et al.*<sup>6</sup> under the name cyclopropenylbenzene, as shown in Fig. 1 (3A, 3B). Previous work has shown that NCD only occurs as an unstable intermediate. In a final attempt to decide the matter, we derived the theoretical PES for NCD under identical conditions to that where the TDA calculations on CHT provide a good account of the observed PES. The NCD theoretical spectrum does not fit the spectrum of Bieri *et al.*<sup>6</sup> Indeed, the reported PES of NCD<sup>6</sup> appears to be an impure form of CHT since almost all bands, except those at 10.2 eV and 18.5 eV, in the two photoelectron spectra are shared.

None of the PES bands of CHT show measurable vibrational structure under current resolution. However, band A with VIE 8.55 eV is not a smooth curve. A sigmoid fit to its leading edge discloses an irregular series of peaks. The most frequent interval, showing a separation of  $80\text{ cm}^{-1}$ , is close to the lowest frequency for the calculated  $1^2A'$  state ( $87.6\text{ cm}^{-1}$ ) at the MP4SDQ level. The absence of observable vibrational structure in band A of the CHT PES is clearly attributable to the high density of low frequency vibrational states. The high frequency vibrations have little effect on the PES and so do not overlay band A beyond a trivial extent.

Our results lead to the conclusions that the PES obtained under our standard conditions is that of CHT and that the ionic VIE sequence is  $1^2A' < 1^2A'' < 2^2A' < 2^2A''$ . The norcaradiene PES remains to be determined, but the theoretical PES does show two low-lying bands, consistent with the strained buta-1,3-diene structure.

## SUPPLEMENTARY MATERIAL

See the [supplementary material](#) for additional information on the following: 1— ${}^1\text{H}$  and  ${}^{13}\text{C}$  NMR spectra. 2—COSY and HSQC spectra unambiguously establishing the assignment of  ${}^1\text{H}$  and  ${}^{13}\text{C}$

NMR signals. 3—Comparison of  ${}^1\text{H}$  NMR experimental data (left) with spectra simulated using the values in Table II (right). 4—60 MHz simulation of  $\text{H}_2-\text{H}_5$  signals using values in Table II (left) compared with the experimental spectrum reproduced from Ref. 19 (right). 5—The singly occupied molecular orbital of the  $1^2A'$  state, which is much more compact than the ground state, with higher bow and stern angles. 6—The transition state for thermal interconversion of CHT to NCD. 7—The HOMO for the transition state for thermal interconversion of CHT to NCD. 8—MP3 and MP4SDQ harmonic vibrational frequencies for CHT compared with anharmonic values at the MP2 level, including rotational constants for the vibrationally excited states, some of which are present in the microwave spectrum. 9—The singly occupied molecular orbital of the  $1^2A'$  state, which is much more compact than the ground state, with higher bow and stern angles. 10—MP4SDQ harmonic vibrational frequencies for the  $1^2A'$  state of CHT. 11—The  $X^2A''$  surface as a function of the two dihedral angles chosen. See the main text for details. 12—A 2-dimensional representation of 11, showing the regular pattern generated as the G-16 “scan” process occurs. See the main text for details. 13—The avoided crossing under  $C_1$  symmetry of  ${}^2A'$  and  ${}^2A''$  states in  $C_5$  symmetry. The energies fitted have been adjusted by adding 269.0 a.u.

## ACKNOWLEDGMENTS

The authors thank the Elettra Synchrotron facility for a grant of beamtime and C. Puglia (Uppsala University, Sweden) and the Carl Tygger Foundation for making available the VG-Scienta SES-200 photoelectron analyzer, the Italian MIUR (under the project PON01-01078/8), and the University of Edinburgh (Eddie3) and Edinburgh Parallel Computing Centre (Cirrus) super-computing facilities for support. Numerical fitting was performed using Gnuplot-5.0.5, and plotting was performed using Origin 7.0, GaussView, and Avogadro.<sup>65-68</sup> The authors thank Professor Malgorzata Biczysko and a reviewer for helpful discussions.

## REFERENCES

- 1 M. H. Palmer, M. Coreno, M. de Simone, C. Grazioli, S. V. Hoffmann, and N. C. Jones, *J. Chem. Phys.* **150**, 194305 (2019).
- 2 M. H. Palmer, S. V. Hoffmann, N. C. Jones, M. Coreno, M. de Simone, and C. Grazioli, *J. Chem. Phys.* **151**, 084304 (2019).
- 3 N. Bodor, M. J. S. Dewar, and S. D. Worley, *J. Am. Chem. Soc.* **92**, 19–24 (1970).
- 4 J. C. Traeger and R. G. McLoughlin, *Int. J. Mass Spectrom. Ion Phys.* **27**, 319–333 (1978).
- 5 T. Bajorek and N. H. Werstiuk, *Can. J. Chem.* **86**, 444–450 (2008).
- 6 G. Bieri, F. Burger, E. Heilbronner, and J. P. Maier, *Helv. Chim. Acta* **60**, 2213–2233 (1977).
- 7 F. Scagnolari, A. Modelli, A. Bottoni, D. Jones, and D. Lazzari, *J. Chem. Soc., Faraday Trans.* **92**, 1447–1453 (1996).
- 8 M. Gower, L. A. P. Kane-Maguire, J. P. Maier, and D. A. Sweigart, *J. Chem. Soc., Dalton Trans.* **1977**, 316–318.
- 9 R. S. Mulliken, C. A. Rieke, and W. G. Brown, *J. Am. Chem. Soc.* **63**, 41–56 (1941).
- 10 A. Streitwieser, *Molecular Orbital Theory for Organic Chemists*, ACS Symposium Series Vol. 1122 (American Chemical Society, 2013), Chap. 9, pp. 275–300.
- 11 I. L. Fragala, J. Takats, and M. A. Zerbo, *Organometallics* **2**, 1502–1504 (1983).

- <sup>12</sup>K. N. Klump and J. P. Chesick, *J. Am. Chem. Soc.* **85**, 130–132 (1963).
- <sup>13</sup>A. A. Jarzecki, J. Gajewski, and E. R. Davidson, *J. Am. Chem. Soc.* **121**, 6928–6935 (1999).
- <sup>14</sup>W. Woods, *J. Org. Chem.* **23**, 110–112 (1958).
- <sup>15</sup>H.-M. Steuhl, C. Bornemann, and M. Klessinger, *Chem. Eur. J.* **5**, 2404–2412 (1999).
- <sup>16</sup>C. Bornemann and M. Klessinger, *Org. Lett.* **1**, 1889–1891 (1999).
- <sup>17</sup>F. A. L. Anet, *J. Am. Chem. Soc.* **86**, 458–460 (1964).
- <sup>18</sup>F. R. Jensen and L. A. Smith, *J. Am. Chem. Soc.* **86**, 956–957 (1964).
- <sup>19</sup>J. B. Lambert, L. J. Durham, P. Lepoutere, and J. D. Roberts, *J. Am. Chem. Soc.* **87**, 3896–3899 (1965).
- <sup>20</sup>H. Günther and R. Wenzl, *Z. Naturforsch.* **22**, 389–399 (1967).
- <sup>21</sup>R. Wehner and H. Günther, *Chem. Ber.* **107**, 3152–3153 (1974).
- <sup>22</sup>M. B. Rubin, *J. Am. Chem. Soc.* **103**, 7791–7792 (1981).
- <sup>23</sup>R. Huisgen, *Angew. Chem., Int. Ed. Engl.* **9**, 751–762 (1970).
- <sup>24</sup>G. Maier, *Angew. Chem., Int. Ed. Engl.* **6**, 402–413 (1967).
- <sup>25</sup>E. Ciganek, *J. Am. Chem. Soc.* **87**, 1149–1150 (1965).
- <sup>26</sup>E. Vogel, W. A. Böll, and H. Günther, *Tetrahedron Lett.* **6**, 609–615 (1965).
- <sup>27</sup>K. G. Torma, K. Voronova, B. Sztáray, and A. Bodi, *J. Phys. Chem. A* **123**, 3454–3463 (2019).
- <sup>28</sup>K. Kimura, S. Katsumata, Y. Achiba, T. Yamazaki, and S. Iwata, *Handbook of HeI Photoelectron Spectra of Fundamental Organic Molecules* (Halsted Press, New York, 1981), p. 189.
- <sup>29</sup>M. J. Frisch, G. W. Trucks, H. B. Schlegel, G. E. Scuseria, M. A. Robb, J. R. Cheeseman, G. Scalmani, V. Barone, G. A. Petersson, H. Nakatsuji, X. Li, M. Caricato, A. V. Marenich, J. Bloino, B. G. Janesko, R. Gomperts, B. Mennucci, H. P. Hratchian, J. V. Ortiz, A. F. Izmaylov, J. L. Sonnenberg, D. Williams-Young, F. Ding, F. Lipparini, F. Egidi, J. Goings, B. Peng, A. Petrone, T. Henderson, D. Ranasinghe, V. G. Zakrzewski, J. Gao, N. Rega, G. Zheng, W. Liang, M. Hada, M. Ehara, K. Toyota, R. Fukuda, J. Hasegawa, M. Ishida, T. Nakajima, Y. Honda, O. Kitao, H. Nakai, T. Vreven, K. Throssell, J. A. Montgomery, Jr., J. E. Peralta, F. Ogliaro, M. J. Bearpark, J. J. Heyd, E. N. Brothers, K. N. Kudin, V. N. Staroverov, T. A. Keith, R. Kobayashi, J. Normand, K. Raghavachari, A. P. Rendell, J. C. Burant, S. S. Iyengar, J. Tomasi, M. Cossi, J. M. Millam, M. Klene, C. Adamo, R. Cammi, J. W. Ochterski, R. L. Martin, K. Morokuma, O. Farkas, J. B. Foresman, and D. J. Fox, *Gaussian 16*, Revision A.03, Gaussian, Inc., Wallingford, CT, 2016.
- <sup>30</sup>M. J. Frisch, M. Head-Gordon, and J. A. Pople, *Chem. Phys. Lett.* **166**, 275–280 (1990).
- <sup>31</sup>M. J. Frisch, M. Head-Gordon, and J. A. Pople, *Chem. Phys. Lett.* **166**, 281–289 (1990).
- <sup>32</sup>R. Krishnan and J. A. Pople, *Int. J. Quantum Chem.* **14**, 91–100 (1978).
- <sup>33</sup>G. W. Trucks, J. D. Watts, E. A. Salter, and R. J. Bartlett, *Chem. Phys. Lett.* **153**, 490–495 (1988).
- <sup>34</sup>R. A. Wheeler and D. C. Spellmeyer, *Annual Reports in Computational Chemistry* (Elsevier, 2010), Vol. 6, p. 124.
- <sup>35</sup>R. O. Ramabhadran and K. Raghavachari, *J. Chem. Theory Comput.* **9**, 3986–3994 (2013).
- <sup>36</sup>G. C. Shields and P. G. Seybold, *Computational Approaches for the Prediction of pKa Values* (CRC Press; Taylor and Francis, 2013), p. 10, ISBN: 978-1-4665-0878-1.
- <sup>37</sup>H.-J. Werner, P. J. Knowles, F. R. Manby, M. Schütz, P. Celani, T. Korona, R. Lindh, A. Mitrushenkov, G. Rauhut, K. R. Shamasundar, T. B. Adler, R. D. Amos, A. Bernhardsson, A. Berning, D. L. Cooper, M. J. O. Deegan, A. J. Dobbyn, F. Eckert, E. Goll, C. Hampel, A. Hesselmann, G. Hetzer, T. Hrenar, G. Jansen, C. Köppl, Y. Liu, A. W. Lloyd, R. A. Mata, A. J. May, S. J. McNicholas, W. Meyer, M. E. Mura, A. Nicklaß, D. P. O'Neill, P. Palmieri, K. Pflüger, R. Pitzer, M. Reiher, T. Shiozaki, H. Stoll, A. J. Stone, R. Tarroni, T. Thorsteinsson, M. Wang, and A. Wolf, *MOLPRO*, version 2012.1, a package of *ab initio* programs, 2012, see <http://www.molpro.net/>.
- <sup>38</sup>H.-J. Werner and P. J. Knowles, *J. Chem. Phys.* **82**, 5053–5063 (1985).
- <sup>39</sup>P. J. Knowles and H.-J. Werner, *Chem. Phys. Lett.* **115**, 259–267 (1985).
- <sup>40</sup>J. V. Ortiz, *Int. J. Quantum Chem.* **105**, 803–808 (2005).
- <sup>41</sup>J. Schirmer and L. S. Cederbaum, *J. Phys. B: At. Mol. Phys.* **11**, 1889–1900 (1978).
- <sup>42</sup>I. H. Hillier, M. A. Vincent, M. F. Guest, and W. von Niessen, *Chem. Phys. Lett.* **134**, 403–406 (1987).
- <sup>43</sup>M. F. Guest, I. J. Bush, H. J. J. Van Dam, P. Sherwood, J. M. H. Thomas, J. H. Van Lenthe, R. W. A. Havenith, and J. Kendrick, *Mol. Phys.* **103**, 719–747 (2005).
- <sup>44</sup>T. H. Dunning, *J. Chem. Phys.* **90**, 1007–1023 (1989).
- <sup>45</sup>R. A. Kendall, T. H. Dunning, and R. J. Harrison, *J. Chem. Phys.* **96**, 6796–6806 (1992).
- <sup>46</sup>M. J. Frisch, J. A. Pople, and J. S. Binkley, *J. Chem. Phys.* **80**, 3265–3269 (1984).
- <sup>47</sup>F. Weigend and R. Ahlrichs, *Phys. Chem. Chem. Phys.* **7**, 3297–3305 (2005).
- <sup>48</sup>F. Weigend, *Phys. Chem. Chem. Phys.* **8**, 1057–1065 (2006).
- <sup>49</sup>S. S. Butcher, *J. Chem. Phys.* **42**, 1833–1836 (1965).
- <sup>50</sup>M. Traetteberg, *J. Am. Chem. Soc.* **86**, 4265–4270 (1964).
- <sup>51</sup>C. la Lau and H. de Ruyter, *Spectrochim. Acta* **19**, 1559–1566 (1963).
- <sup>52</sup>J. D. Dunitz and P. Pauling, *Helv. Chim. Acta* **43**, 2188–2197 (1960).
- <sup>53</sup>J. M. Schulman, R. L. Disch, and M. L. Sabio, *J. Am. Chem. Soc.* **104**, 3785–3788 (1982).
- <sup>54</sup>R. E. Davis and A. Tulinsky, *Tetrahedron Lett.* **3**, 839–846 (1962).
- <sup>55</sup>J. O. Jensen, *J. Mol. Struct.: THEOCHEM* **724**, 1–8 (2005).
- <sup>56</sup>C. Peng and H. Bernhard Schlegel, *Isr. J. Chem.* **33**, 449–454 (1993).
- <sup>57</sup>C. Peng, P. Y. Ayala, H. B. Schlegel, and M. J. Frisch, *J. Comput. Chem.* **17**, 49–56 (1996).
- <sup>58</sup>R. B. Woodward and R. Hoffmann, *J. Am. Chem. Soc.* **87**, 395–397 (1965).
- <sup>59</sup>R. B. Woodward and R. Hoffmann, *Angew. Chem., Int. Ed. Engl.* **8**, 781–853 (1969).
- <sup>60</sup>E. N. Marvell, G. Caple, B. Schatz, and W. Pippin, *Tetrahedron* **29**, 3781 (1973); E. N. Marvell, G. Caple, and B. Schatz, *Tetrahedron Lett.* **6**, 385 (1965); B. M. Jacobson, G. M. Arvanitis, C. A. Eliassen, and R. Mitelman, *J. Org. Chem.* **50**, 194 (1985); J. A. Duncan, D. E. G. Calkins, and M. Chavarha, *J. Am. Chem. Soc.* **130**, 6740 (2008).
- <sup>61</sup>T. A. Keith, AIMAll (Version 19.10.12), TK Gristmill Software, Overland Park, KS, USA, 2019, [aim.tkgristmill.com](http://aim.tkgristmill.com).
- <sup>62</sup>R. F. W. Bader, *Atoms in Molecules: A Quantum Theory* (Oxford University Press, Oxford, 1990).
- <sup>63</sup>R. F. W. Bader, *Acc. Chem. Res.* **8**, 34 (1975).
- <sup>64</sup>R. F. W. Bader, *Chem. Rev.* **91**, 893 (1991).
- <sup>65</sup>See <http://avogadro.cc/> for Avogadro: An open-source molecular builder and visualization tool, version 1.XX.
- <sup>66</sup>R. Dennington, T. A. Keith, and J. M. Millam, GaussView, Version 6.1, Semichem, Inc., Shawnee Mission, KS, 2016.
- <sup>67</sup>Origin Version 2019, OriginLab Corporation, Northampton, MA, USA.
- <sup>68</sup>See <http://www.gnuplot.info/> for Gnuplot Release 5.0.7.